PAPER

Check for updates

Epoxy-based vitrimeric semi-interpenetrating network/MXene nanocomposites for hydrogen gas barrier applications†

Anandarup Bhattacharyya, [ID] [a] Subhabrata Saha,[a,b] Sambedan Jena,[a] Hoang Tuan Nguyen, [ID] [a] Duy Thanh Tran, [ID] [a] Nam Hoon Kim [ID] *[a,d] and Joong Hee Lee [ID] *[a,c,d]

Herein, we report MXene-filled epoxy-based vitrimeric nanocomposites featuring a semi-interpenetrating network (S-IPN) to develop a hydrogen gas (H_2) barrier coating with self-healing characteristics for compressed H_2 storage applications. The reversible epoxy network was formed by synthesizing linear epoxy chains with pendent bis-hydroxyl groups using amino diol, which were then crosslinked with 1,4-benzenediboronic acid to generate dynamic boronic ester linkages. To achieve the S-IPN-type molecular arrangement, the epoxy chains were *in situ* crosslinked in the presence of poly(ethylene-*co*-vinyl alcohol) (EVOH), giving rise to a self-healing network (EEP) with a healing efficiency of 87%. Into the S-IPN vitrimer (EEP), a 2D platelet-type nanofiller MXene was incorporated to introduce a tortuous path for H_2 gas diffusion along with improved mechanical properties. The nanocomposite coating was applied to nylon 6 liner material, which is conventionally used in all-composite H_2 storage vessels. The application of a 2 wt% MXene/EEP nanocomposite coating showed a permeability coefficient of 0.062 cm^3 mm m^{-2} d^{-1} atm^{-1} exhibiting ~96% reduction in gas permeability compared to uncoated nylon 6. The same nanocomposite exhibited a healing efficiency of 79%. Increasing the MXene loading to 10 wt% further reduced the permeability coefficient to 0.002 cm^3 mm m^{-2} d^{-1} atm^{-1}; however, the healing efficiency decreased due to restricted chain mobility. In essence, the current work highlights the potential of vitrimeric S-IPN nanocomposite coatings for H_2 gas-barrier applications, enhancing safety and performance.

1 Introduction

Hydrogen, with a small kinetic radius and scarcity on this planet, presents upfront challenges for its gaseous storage, which is crucial for advancing the hydrogen economy. For onboard storage of H_2 in fuel-cell vehicles, state-of-the-art type IV all-composite pressure vessels featuring a polymeric liner overwrapped with a carbon fiber outer layer are preferred over metallic vessels, as the former exhibit characteristics of lightweight, high specific strength, and resistance to hydrogen embrittlement.[1,2] With its strong intra/inter-molecular hydrogen bonding, and high crystallinity, nylon 6 appears to be an efficient liner material for type IV H_2 storage vessels.[3] However, the high-pressure requirement (350 to 700 times atmospheric pressure) during gaseous storage leads to saturation of H_2 in the liner layer, eventually causing stress whitening, blistering, buckling, and delamination due to decompression failure.[4] Hence, a barrier coating on the inner side wall of the liner to suppress gas diffusion is pertinent.[5] To achieve efficient gas-barrier properties, the free volume of the coating layer, the adhesion strength of the coating with the liner material, and the introduction of long tortuous paths play a pivotal role.[6] The first two factors are achieved by the polymer and the tortuosity is governed by the nanofiller being subjected to physical or chemical bond formation with the polymer matrix.[7,8]

With linear semicrystalline polymers used in gas-barrier applications,[9,10] gases predominantly diffuse through the amorphous regions while the crystalline domains are usually impermeable due to their compact molecular geometry.[11] Ethylene vinyl alcohol copolymer (EVOH) is a promising semi-

[a]Department of Nano Convergence Engineering, Jeonbuk National University, Jeonju, Jeonbuk, 54896, Republic of Korea. E-mail: nhk@jbnu.ac.kr, jhl@jbnu.ac.kr
[b]Manufacturing Science Division, Oak Ridge National Laboratory, Knoxville, TN, 37932, USA
[c]Carbon Composite Research Centre, Department of Polymer & Nanoscience and Technology, Jeonbuk National University, Jeonju, Jeonbuk, 54896, Republic of Korea
[d]AHES Co., 445 Techno Valley-ro, Bongdong-eup, Wanju-gun, Jeonbuk, 55314, Republic of Korea

†Electronic supplementary information (ESI) available: Synthesis procedure for MXene ($Ti_3C_2T_x$), images of spray-coated nylon 6 substrates of polymer nanocomposites, adhesion test images for coated nylon 6 substrates, atomic wt% results from XPS, and a table of comparison for H_2GTR and permeability coefficients for 2D nanofiller-reinforced polymer nanocomposites. See DOI: https://doi.org/10.1039/d4nr04702h

crystalline thermoplastic with such barrier properties due to its high crystallinity.[12–14] Our previous publication suggested that a significant reduction in H_2 gas permeability occurs when EVOH in combination with graphene oxide (GO) and boric acid was applied to the nylon 6 liner.[15] Again, the non-polar hydrogen molecules undergo unfavorable polymer-penetrant interactions with polar polymers, such as EVOH.[16] Thus, the adsorption of hydrogen by the formation of sorbed cages is less favorable in EVOH. However, crystalline polymers typically exhibit weaker adhesion, which is also a critical factor for barrier coatings. To address this, we recently revealed that a semi-interpenetrating network (S-IPN) comprising epoxy and TPU exhibited a judicious combination of adhesion and gas-barrier properties because of the formation of a dense network.[17,18] Subsequently, we have developed an S-IPN with EVOH and epoxy for H_2 gas-barrier coatings with the added benefits of high adhesive strength and higher density in the amorphous regions. However, instead of permanent covalent crosslinking, the effect of dynamic covalent bonds has been explored here for crosslinking the epoxy phase to develop a self-healable coating.

In previous years, exemplary works on vitrimers[19–23] consisting of reversible covalent bonds utilizing Diels–Alder adducts,[24] transesterification,[25] metathesis[22] etc., appear to be promising materials for composites offering self-healing and recycling characteristics. For reversible bond formation, soft polymeric materials like hydrogels and elastomers offer additional advantages owing to their high chain mobility.[26,27] In contrast, the dynamic covalent bond formation within rigid thermosetting polymers, such as phenolic and epoxy resins, is challenging because of limited chain mobility.[28] Recently, Yang et al., focusing on boronic acid-based crosslinking, explored the metathesis kinetics of boronic esters derived from catechol incorporated into polyurethane (PU) networks to establish PU elastomeric vitrimers.[29] The catechol moieties were prepared using solution casting of linear PUs inheriting catechol and 1,4-phenylenediboronic acid as pendant groups. The aqueous and alcohol medium used to hydrolyze boronate esters to initiate bond reformation, also facilitates the chain mobility contributing to the reformation of covalent bonds even in the case of rigid polymers.[30] Wang et al. reported the use of boronic acid to recycle novolac resin (i.e. phenolic resin) triggered by the alcoholysis reaction.[31] Organoboronic acids have been extended to form dynamic B–O bonds to design bulk-healable and reprocessable polymeric materials by associative/dissociative bond exchange methods through ring-opening metathesis reactions.[32,33] Recently, Ito et al. reported an elastomeric epoxy network by combining poly(n-butyl methacrylate-co-4-vinylphenyl boronic acid) with a linear epoxy chain containing 2,2-bis(4-glycidyloxyphenyl)propane and 1-propylamine.[34] The formation of reversible crosslinks between the boronic acid group of the acrylate copolymer and the amine diol of the linear epoxy allowed the metathesis reaction to exhibit dynamic covalent bonding. In contrast, our approach is simplified by utilizing 3-amino-1,2-propanediol (APD) to synthesize linear epoxy chains, which are then cross-linked with bis-boronic acid (BDB) at a molar ratio of 2 : 1 amine diol : BDB. By leveraging the metathesis reaction of the boronic ester linkage, the epoxy system is susceptible to bond reformation at elevated temperatures to induce self-healing properties while at the same time maintaining its structural integrity under ambient conditions.

To introduce a long tortuous path in barrier coatings, two-dimensional (2D) platelet-type nanofillers show promising results.[14,35–37] The 2D MXene nanofiller, comprised of metal carbides/nitrides/carbonitrides, has emerged as a potential choice for gas-barrier applications. Tang et al. reported a 2D MXene/nanocellulose self-assembled film to improve oxygen barrier properties.[38] Shi et al. investigated MXene-based H_2-barrier coatings for steel pipelines.[39] In our earlier work, we also assessed the H_2 gas-barrier properties of MXene, which showed promising results.[9,18] MXene layers not only enhance tortuosity,[40] but also trap hydrogen within the crystalline lattice through Kubas-type interactions, thus preventing it from diffusing into the liner layer of the storage vessel.[41,42] Additionally, the surface of MXene contains hydroxyl groups capable of interacting with boronic acid to improve the polymer–filler interaction. Considering these advantages, MXene was introduced into the present work in combination with the EVOH/epoxy dynamically crosslinked S-IPN network.

A solution-blending approach was taken to design a reversible S-IPN composite containing 1 : 1 weight ratio of EVOH and epoxy vitrimer in combination with MXene. The entire suspension of EVOH/epoxy and MXene was spray-coated on a nylon 6 substrate, the very material used as a liner in H_2 storage tanks. This called for the formation of a dense barrier layer network during the in situ curing of epoxy in the presence of EVOH. The coated substrates were evaluated for H_2 gas-barrier properties at ambient temperature. All the nanocomposites were characterized in depth. Furthermore, the formation of self-healing networks at the bulk level was reasoned and tested under suitable temperature conditions for the as-prepared boronic ester bonds. The dynamic behavior of these boronic ester crosslinks bolstered the polymer chain networks for bulk-level healing, suggesting their usage in high performance coating materials for H_2 storage tanks.

2 Methods

2.1 Materials

EVOH (ethylene content 32 mol%) pellets having a density of 1.19 g mL^{-1} at 25 °C, were acquired from Sigma Aldrich (USA). Diglycidyl ether of bisphenol A type (DGEBA, epoxy primer with an epoxy equivalent weight of ~170 g mol^{-1}) with a density of 1.16 g mL^{-1}, and 3-amino-1,2-propanediol (APD) (amine equivalent weight of 45.5 g mol^{-1}) were purchased from Sigma Aldrich (USA) and Thermo Fisher Scientific (USA), respectively. A nylon 6 sheet (thickness ~3.84 mm) was obtained from ILJIN HYSOLUS, Republic of Korea, and was used as a substrate for the polymer nanocomposite coating. Nylon 6 film (thickness ~270 μm) was procured from

Goodfellow Cambridge Limited (UK) to investigate the mechanical properties of the coating. 1,4-Benzenediboronic acid (BDB) and molecular sieves (pore size 3 Å) in the form of beads, were procured from Alfa Aesar (USA). The MAX (Ti_3AlC_2) phase was obtained from Laizhou Kai Kai Ceramic Materials Co. Ltd, China. Lithium fluoride (LiF) was purchased from Alfa Aesar (USA). Hydrochloric acid (HCl), dimethyl sulfoxide (DMSO), and ethanol were obtained from standard sources. All the reagents mentioned above were of analytical grade and used without any further purification.

2.2 Synthesis of S-IPN film comprised of EVOH/epoxy vitrimer (EEP)

The synthesis of the S-IPN to develop the matrix for the barrier coating involves two successive steps: 1. synthesis of the linear epoxy chain, and 2. dynamic crosslinking of the epoxy chain in the presence of EVOH, leading to the formation of the S-IPN structure. To form the linear chain in the first step, the epoxy monomer DGEBA was mixed with APD at a stoichiometric ratio by solution mixing. A fixed amount of DGEBA was dissolved in DMSO with constant stirring at 60 °C for 3 h to achieve a homogeneous solution of concentration 50 mg mL^{-1}. Into the solution, an equivalent amount of APD was added and stirring was continued for 24 h at 60 °C, leading to the formation of linear epoxy chains by the reaction between the reactive amine group of APD molecules and the epoxy end groups of DGEBA molecules. The linear epoxy chains thus formed contain pendent bis-hydroxyl groups from the APD moieties that are further involved in the reversible crosslink formation in the later stage. In the second step, an equivalent amount of BDB was added to the DGEBA/APD solution and stirred for 72 h at 60 °C to allow the formation of reversible boronic ester linkages. To accelerate the boronic ester formation, molecular sieves were also added at the beginning of the second stage reaction to absorb water molecules formed as by-product. It is to be noted that the weight ratios of DGEBA (72% w/w), APD (16% w/w), and BDB (12% w/w) were maintained throughout the synthesis. Finally, an EVOH solution in DMSO, prepared separately, was mixed with the epoxy solution at 1 : 1 weight ratio for 24 h at 25 °C before being solvent cast onto a Teflon Petri dish. The solution was then dried under vacuum at 60 °C and thereafter cured at 80 °C for 3 h, resulting in the formation of the S-IPN with dynamic covalent crosslinking, defined as EEP. In this work, a 1 : 1 ratio of EVOH and epoxy was chosen, as higher loading of epoxy can lead to a brittle coating that is undesirable for barrier applications. However, future work will focus on the optimization of the EVOH : epoxy ratio to improve both barrier and mechanical properties.

2.3 Synthesis of EEP-nanocomposites with MXene/S-IPN vitrimer

To develop the nanocomposite, MXene was first synthesized by selectively etching out aluminum (Al) from the MAX phase using HF, which was *in situ* prepared from LiF/HCl. The entire procedure for synthesizing MXene is mentioned in the ESI.† The synthesized freeze-dried MXene was then ground using an

agate mortar and pestle, followed by dispersion in DMSO (concentration ~1 mg mL^{-1}) under an inert N_2 atmosphere *via* ultra-sonication for 30 min. After that, the required amount of dispersed suspension was added into the EVOH/epoxy solution as mentioned earlier and stirred for another 30 min before being poured into the Teflon Petri dish to prepare the solvent-cast nanocomposite film. The concentration of MXene in the nanocomposite film was varied at 2, 5, and 10 wt% designated as EEP-2 MXene, EEP-5 MXene, and EEP-10 MXene, respectively. For all the solvent-cast nanocomposite films, including the unfilled film, the total weight of the polymer was kept at 1 g.

2.4 Preparation of coated nylon 6 substrate with unfilled and filled EEP

To investigate the H_2 gas-barrier properties, nylon 6 substrates of ~3.85 mm thickness were coated with the as-prepared unfilled EEP and EEP/MXene solutions described previously. Similar to the solvent-cast films, the concentration of MXene was varied at 2, 5, and 10 wt% to develop the nanocomposite coating. However, the total weight of the coating for all compositions was maintained at 450 mg, unlike the cast films. The coating was applied to the nylon 6 substrate using a scalable spraying method. While spraying, the nozzle was kept at a constant height and the temperature was maintained at around 100 °C, enabling efficient drying during the coating process. After the substrates were coated, all the coated samples were kept in a vacuum oven at 60 °C for 20 h for complete drying. At the final stage, the coated samples were exposed to curing at 80 °C for 3 h in a vacuum oven. To investigate the mechanical properties of the coating, EEP and EEP-10 MXene nanocomposite were coated onto thin nylon 6 films of thickness ~0.3 mm, while the the subsequent process for preparing the coating remained similar.

2.5 Characterization

To characterize MXene, Fourier-transform infrared (FTIR) spectroscopy was performed using a Nicolet 6700 spectrometer (ThermoScientific, USA) while keeping the spectral range within 500–4000 cm^{-1} under ambient conditions. The attenuated total reflectance (ATR-FTIR) Spectroscopy mode was used for the film samples within the range of 400–4000 cm^{-1} on a PerkinElmer Spectrum 400 spectrometer (Waltham, MA, USA). X-ray photoelectron spectroscopy (XPS) was conducted using a Theta Probe Instrument (Thermo Fisher Scientific, UK) at KBSI (Jeonju Centre) for analysis of the nanofillers. The wide-angle X-ray diffraction (WAXD) method was used for both the nanofillers and polymer nanocomposites, where the total scan was limited to 1946 steps having an incremental size of 0.0330° and a scanning time per step of 0.59 s. The dynamic mechanical performance of solvent-cast films and coated nylon films was investigated using a DMA Q800 (WATERS, USA) where the test conditions were maintained at a frequency of 1 Hz, strain amplitude of 10^{-3} mm, and temperature ranging from −50 to 140 °C at a heating rate of 5 °C min^{-1}. The solvent-cast films were also analyzed by differential scanning calorimetry (DSC) using a DSC Q20 (WATERS, USA). The

testing conditions were maintained at a heating/cooling rate of 5 °C min^{-1} under an inert N$_2$ atmosphere. The first heating cycle ranged from −50 to 250 °C followed by the first cooling cycle from 250 to −50 °C. The second heating cycle was run again from −50 to 250 °C. The first heating cycle was initiated to remove any residual thermal history in the films. The glass transition temperature (T_g) for all the films was obtained from the second heating cycle. The morphology was investigated by field emission scanning electron microscopy (FESEM) using a Supra 40 instrument (Zeiss, Germany) provisioned with an energy dispersive X-ray (EDX) detector (Oxford Instruments, UK), and by atomic force microscopy (AFM) using an NX10 Park System (South Korea). To investigate the nanofiller morphology, FESEM was performed by drop-casting a dilute suspension (0.01% w/v) on silicon wafers. The self-healing characteristics of solvent-cast films were monitored by notching the dry films with a sharp razor followed by investigating the scratch area using FESEM and AFM. For both FESEM and AFM, the same samples were used. Before performing the FESEM, the surface was sputter-coated with platinum for 120 s to avoid charge accumulation. At the beginning of the healing reaction, water droplets were applied to the cut surface to ensure the hydrolysis of dioxaborolane linkages. Once the water evaporated, the dry nanocomposite films were kept in a vacuum oven at 140 °C for 2 h followed by maintaining the temperature at 90 °C for another 12 h. Finally, the films were brought to ambient temperatures and the same samples were examined using FESEM and AFM to investigate the healing performance. AFM scanning was conducted in tapping mode where the set point (varied as per sample thickness) and scan rate were kept at 9.2 nm and 0.6 Hz, respectively. For examining the tensile strength and Young's modulus of the solvent-cast films and coated nylon 6 films, a tensile test was run on a DUT-500C device (Daekyung Engineering, Korea) using a 5 kN load cell. The solvent-cast films and coated nylon 6 films were exposed to an extension rate of 2 mm min^{-1} and 10 mm min^{-1}, respectively, under ambient conditions.

The H$_2$ gas-transmission rate (H$_2$GTR) was assessed for both the uncoated and coated nylon 6 substrates using a GDP-C (Brugger Feinmechanik GmbH, Germany) gas permeability machine under 100 kPa pressure and 25 °C test conditions. The dust and grease from the circular testing area of diameter 2.5 cm were removed completely. Using GDP-C software, the H$_2$GTR was calculated from the following equation:

$$\text{GTR} = \frac{\ln\left(\frac{p_{n+1} - p_n}{p_n - p_\infty} + 1\right)V}{dt \times a \times T \times R_m} \tag{1}$$

Here, p_n is the test-chamber pressure (bottom side of the tested substrate) at time n, p_∞ is the pressure on the top side of the substrate (∼100 kPa) (where H$_2$ was purged), V represents the test-chamber volume in cm^3, dt is the time difference between n and $(n + 1)$ expressed in days (d), a is the test area in m^2, T is the temperature inside the test chamber in K, and R_m is the universal gas constant (R/molar volume V_m =

0.00371 bar K^{-1}) under standard conditions. The evacuation process of the test chamber was conducted for 10 h so that all residual gases and moisture from the test chamber could be removed before the analysis. Hence, the gas permeability was measured at 0% humidity. However, the room's humidity was maintained at 40%. The testing of H$_2$GTR was conducted for 20 h at ambient temperature. Furthermore, H$_2$GTR of the EEP-coated nylon 6 was also measured at 50 °C. At the initial time of testing, equilibrium was not attained. At the later stage, a consistency in the H$_2$GTR plots was observed and an average value was taken from the last 5 h of the test. For calculating the permeability coefficient (P_1) of the coated layer on the nylon 6 substrate, the Henis and Tripodi resistance model was used, and the following equation was implemented:[43,44]

$$\frac{J}{\Delta P} = \frac{P}{l} = \left(\frac{l_1}{P_1} + \frac{l_2}{P_2}\right)^{-1} \tag{2}$$

The ($J/\Delta P$) term denotes the permeation rate per pressure difference across the composite-coated sheet (GTR), P is the total permeability of the coated nylon 6 sheet, and l is the total thickness of the coated nylon 6 sheet. The terms l_1 and l_2 are the thickness of the barrier coating and nylon 6, respectively. The P_2 term is denoted as the permeability coefficient of the uncoated nylon 6 sheet. To investigate the adhesion strength, a peel-off test was conducted as per the ASTM standard D3359-17. The coating surface was incised into 2 × 2 mm^2 grids using a sharp blade. Scotch tape was pressed on the notched surface for 30 s, and subsequently peeled off. The water contact angle (WCA) at 25 °C was measured by using a DSA30S drop shape analyzer (Krüss, Germany).

3 Results & discussion

Fig. 1 demonstrates the systematic route to preparing a gas-barrier coating with a reversibly crosslinked S-IPN aiming to reduce H$_2$ transmission through a nylon 6 liner. The reversible network was achieved by crosslinking the linear epoxy (ii) with bis-boronic acid through pendent diol groups of amine forming boronic ester linkages (iii). Leveraging the metathesis reaction of boronic ester (iv), the developed epoxy network provides self-healing characteristics to the coating showing the potential to improve the life cycle of the barrier layer. The pendent hydroxyl groups of the EVOH molecule formed strong covalent and hydrogen-bonded interactions with the epoxy (EP)/APD/BDB complex (v) contributing to a dense architecture that improved the barrier properties. The added MXene is also involved in bonding interactions with the boronic ester group forming strong polymer–filler linkages (vi), which further suppressed gas transmission by increasing the tortuosity of the coating.

3.1 Characterization of vitrimeric S-IPN with reversible crosslinking

To understand the formation of dioxaborolane linkages, FTIR spectroscopy was performed on the unfilled S-IPN film (EEP
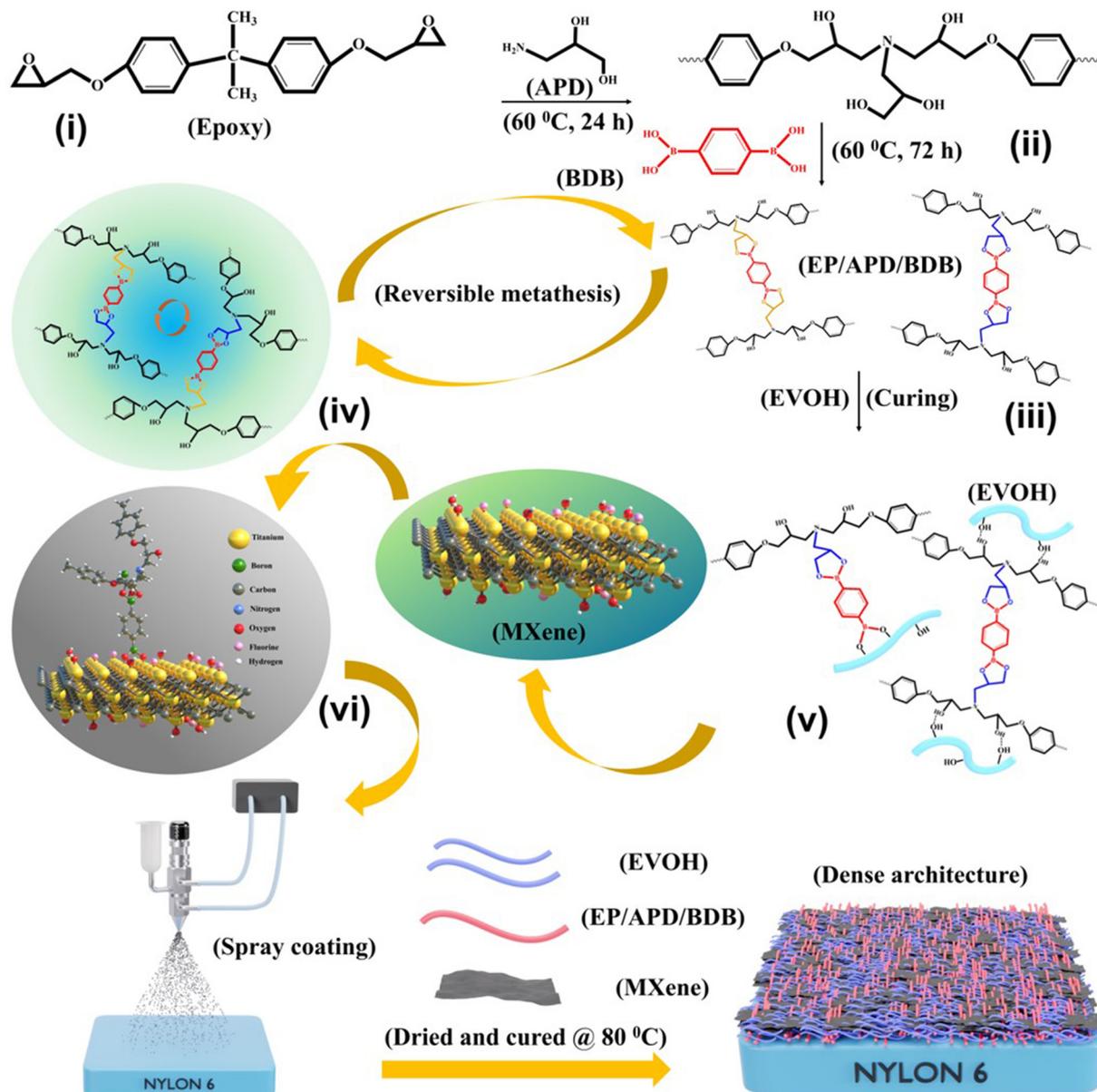
Fig. 1 Schematic of the development of a dense architecture nanocomposite coating comprised of MXene-reinforced EVOH/epoxy S-IPN vitrimer for H$_2$ gas-barrier applications.

film) and to further verify the reversible bond formation, FTIR spectra of the film were recorded after dipping it into DI water for 6 h designated as EEP (wet) (Fig. 2a). The EEP film showed the characteristic peaks for –OH stretching (~3310 cm^{-1}), –CH stretching (~2924 and 2852 cm^{-1}), –CN (~1241 cm^{-1}), and C=C aromatic (~1505 cm^{-1}) ring stretching, indicating the existence of EVOH and epoxy chains.[45] Moreover, the peaks corresponding to B–O–C (~1335 and ~1416 cm^{-1}),[46–48] B–O (~1361, ~1383 and ~827 cm^{-1})[45,47,48] and B–C stretching (~1085 cm^{-1})[45] vibration peaks implied the formation of dioxaborolane linkages. Meanwhile, on dipping the EEP film into DI water, the boronic ester linkages encountered hydrolysis causing partial leaching of the BDB molecule resulting in the

weakening or broadening of the peaks corresponding to B–O–C, B–O and B–C stretching vibrations, suggesting the reversible bonding. However, the BDB molecule is susceptible to reacting with both the linear epoxy chains containing pendent dihydroxyl groups and the EVOH molecules,[49] which is very difficult to understand from the FTIR spectra. To investigate this, we first immersed the film in DMSO at 60 °C for 24 h aiming to dissolve the free EVOH molecules. Fig. 2b, c, and Fig. S1,† show the FESEM images of the EEP films before and after immersion into DMSO, respectively. The initially smooth surface of the film appeared rough after immersion in DMSO. A 25% reduction in weight was noted instead of complete dissolution of EVOH, and the film's integrity was also retained.
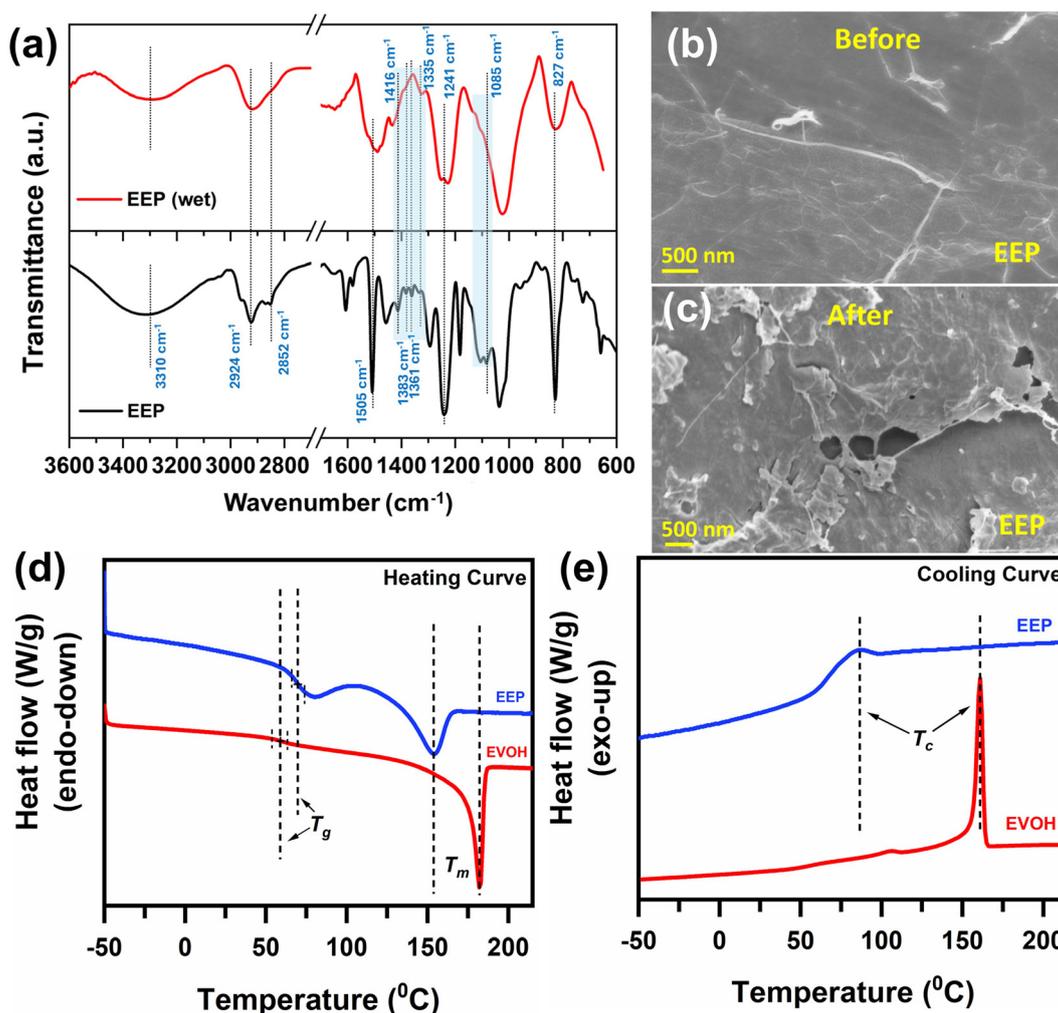
Fig. 2 (a) FTIR spectra of EEP wet and dry films; (b) and (c) FESEM images of the EEP film before and after dipping into DMSO, respectively; (d) and (e) DSC endotherm and exotherm, respectively, of EVOH and EEP films.

This clearly indicates the formation of S-IPN (a bound molecular architecture), which could otherwise result in the disintegration of the film. The reduction in weight indicates the fraction of unbound EVOH molecules. The formation of S-IPN is further understood from the DSC analysis as shown in Fig. 2d and e. The pristine EVOH film showed a melting peak at 182 °C in the DSC endothermic curve, which significantly reduced to 153 °C in the case of EEP (Fig. 2d). On the other hand, T_g shown by the inflection point in the endothermic curve became more distinct for EEP as compared to pristine EVOH (58 °C) and it also increased (67 °C) with the addition of epoxy. The crystallization peak of EVOH (161 °C), as appeared in the DSC exothermic curve (Fig. 2e), shifted to a lower temperature (86 °C) in the case of EEP. The results are attributed to the formation of the S-IPN network, which partially immobilized EVOH molecules hindering chain folding to form crystals. Consequently, crystal formation was delayed, and it suppressed the formation of larger crystals, resulting in a depletion of both crystallization and melting temperatures. In

contrast, the glass transition temperature increased due to the restricted chain mobility of EEP caused by the crosslinked epoxy molecules, which in turn escalated the barrier properties of the film, as will be discussed later.

Self-healing behavior was investigated from the extent of recovery of the applied scratches on the film sample using FESEM and AFM. Healing was initiated by the hydrolysis of boronic ester linkages followed by bond reformation at elevated temperatures. A temperature of 140 °C was maintained during preconditioning based on the onset of the melting temperature of EEP (Fig. 2d) so as to induce the flowability of the polymer chains. A scratch of width 5 μm was observed in the FESEM image before the healing test (Fig. 3a). After healing, the recovery of the scratch was clearly detected across the span of the crack indicating the flow of S-IPN polymer chains and probable rejoining of the dioxaborolane moieties. Furthermore, the AFM height image quantified the depth of the cuts recovered after the healing process (Fig. 3b). The same samples were compared using FESEM and AFM before and
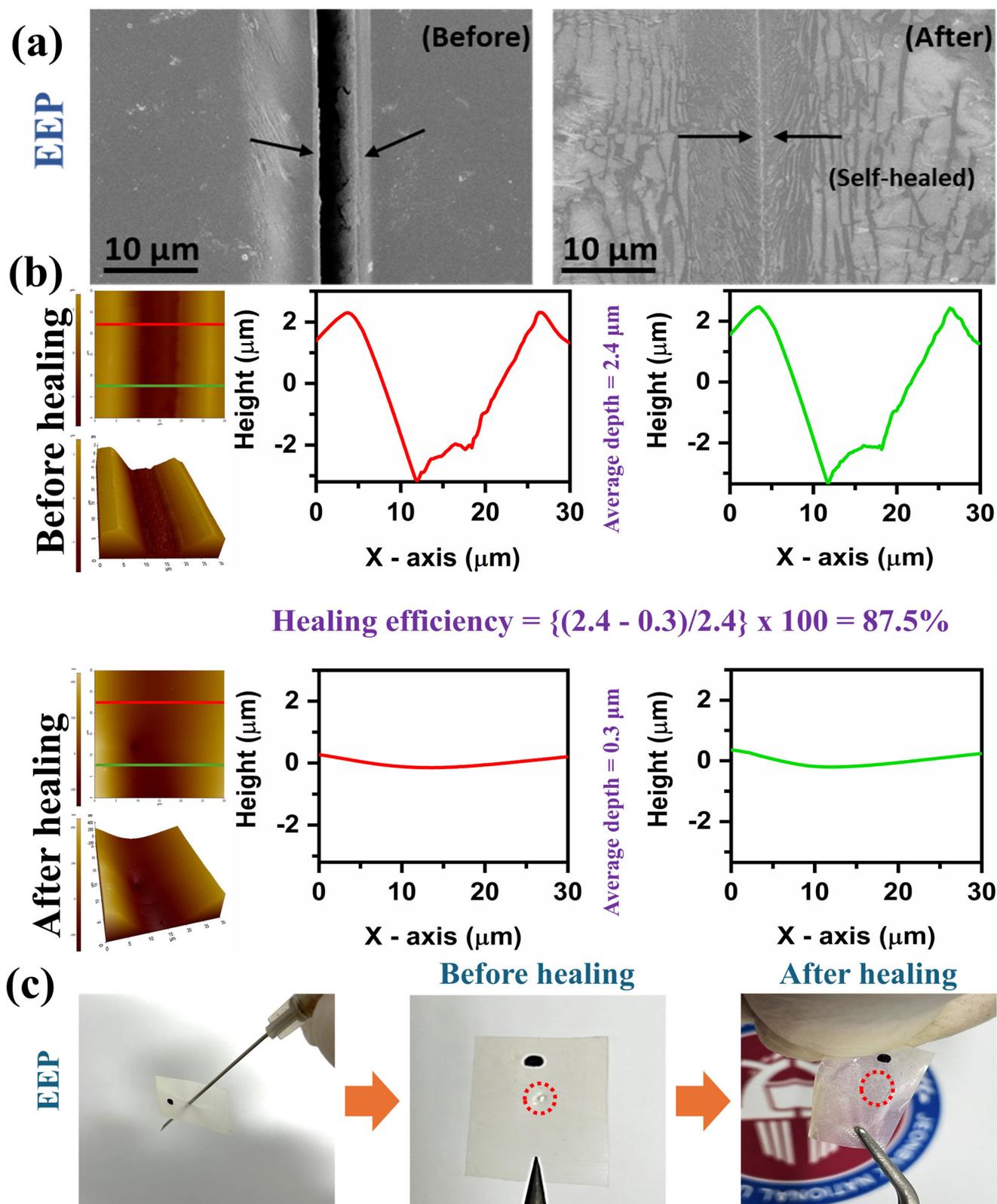
Fig. 3 (a) FESEM images of the EEP film samples before and after the healing test; (b) AFM height image of the EEP film before and after the healing test showing the depth of the damaged area; (c) perforation test of the EEP film showing the healing of the damaged area.

after the healing test. As shown in Fig. 3b, the height images of the surface scratch before and after the healing stages of EEP were captured and confirmed the observations obtained from the FESEM analysis. Two different areas on the height topography were chosen to understand the height variation across the crack span. The average depth of the cut before healing was 2.4 μm, which significantly reduced to 0.3 μm showing a considerable recovery of 87.5% after healing. A perforation test was also performed on the EEP film, as depicted in Fig. 3c, where the film was punctured with a needle to create a hole. After performing the same healing process mentioned earlier, the damaged area in the EEP film was found to be healed even after applying manual stretching, emanating from the dynamic crosslinking behavior of the boronic esters.[32]

3.2 Characterization of the MXene-filled S-IPN nanocomposites

The mechanical properties of the solvent-cast nanocomposite films containing 2, 5 and 10 wt% MXene were compared with the unfilled S-IPN (EEP) and pristine EVOH films as shown in Fig. 4a and b. The unfilled EEP film had a tensile strength of 28 MPa and a Young's modulus value of ~618 MPa exhibiting ~22% and ~81% increments in tensile strength and modulus, respectively, as compared to the pristine EVOH film. The improvement in the mechanical properties with the addition of epoxy into EVOH again supported the formation of S-IPN, which restricted chain mobility, leading to an increase in

modulus at the cost of elongation at break. The incorporation of MXene further enhanced the tensile modulus significantly up to 5 wt% loading (i.e., ~875 and ~990 MPa for EEP-2 MXene and EEP-5 MXene, respectively) and after that the modulus marginally increased to ~1005 MPa for EEP-10 MXene. These results suggested that the optimal modulus was achieved at 5 wt% MXene loading. On the other hand, the tensile strength of the nanocomposite exhibited an increment of 20% at 2 wt% MXene concentration as compared to the unfilled EEP film. Furthermore, the increase in the nanofiller content was related to a gradual drop in tensile strength, due to a considerable reduction in elongation at break. The increasing stiffness of the S-IPN structure in the presence of MXene suppressed the elongation at break for all the nanocomposites, specifically at 10 wt% MXene concentration leading to a drastic reduction. The improvement in modulus combined with reduced elongation at break implied the adsorption of the EEP chain onto the MXene surface.

An increase in the glass transition temperature was also observed in the DSC endotherm (Fig. 4c) indicating the restricted chain mobility upon the addition of MXene. Compared to that in the unfilled EEP, T_g increased to 73 °C, 76 °C, and 97 °C for EEP-2 MXene, EEP-5 MXene, and EEP-10 MXene, respectively. The crystallization of the EVOH molecules was further impaired in the presence of MXene due to the increasing hindrance in chain folding, thus indicated by a weak melting peak. DMA analysis of the nanocomposite films revealed a shift in the tan delta peak to higher temperatures
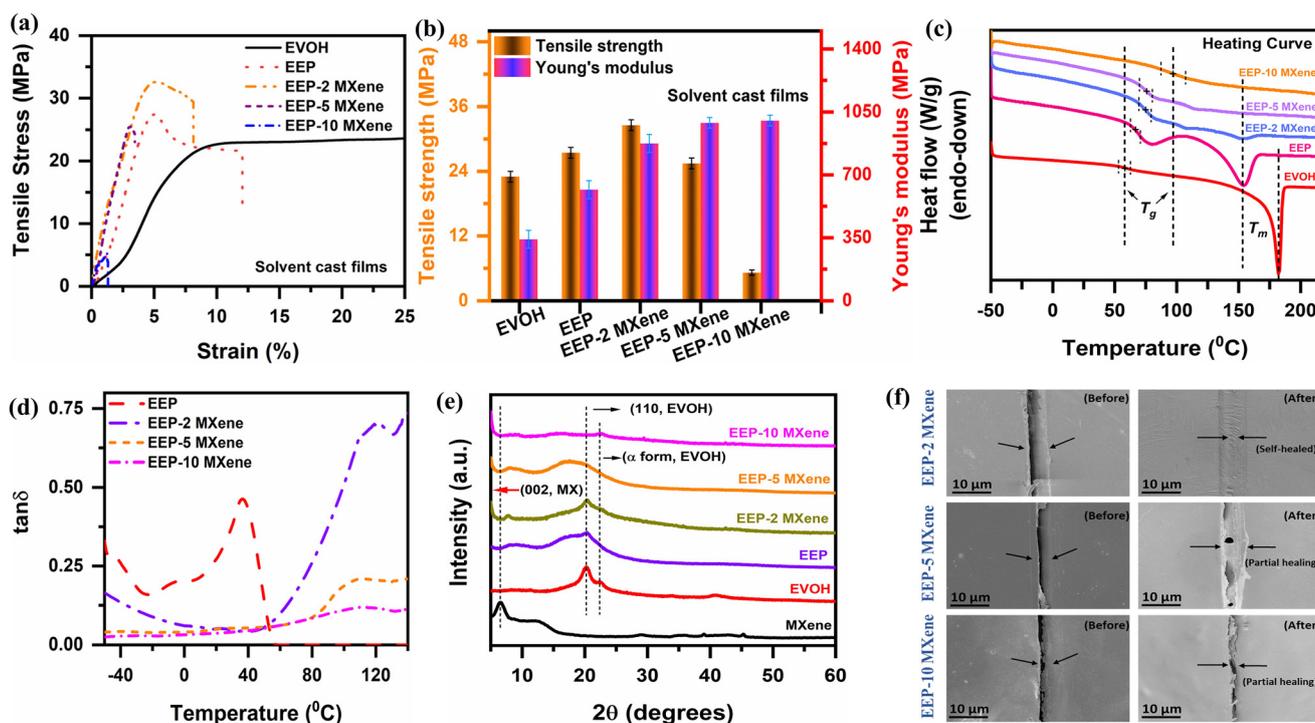

Fig. 4 Properties of the solvent–cast nanocomposite films: (a) and (b) mechanical properties; (c) DSC heating scan; (d) tan δ obtained from DMA; (e) WAXD analysis; (f) FESEM images of the nanocomposite films before and after healing.

with the incorporation of MXene (Fig. 4d), represented by an increase in T_g in line with the DSC analysis. All the above results manifested strong interaction between the MXene and the S-IPN molecules, further supported by the WAXD analysis (Fig. 4e). The characteristic MXene peak of the (002) plane at $2\theta = 6.5°$ shifted to a lower angle (~5°) for the nanocomposites illustrating the interaction that resulted in layer separation.[9,50] Besides, the EVOH (110) peak gradually broadened with the addition of the nanofiller, attributed to the reduced crystallinity due to the restricted motion of the chains.[51] The adsorption of the EEP chain on the MXene surface altered the healing characteristics of the nanocomposite films as the healing mechanism is kinetically controlled. Fig. 4f delineates FESEM scans showing the healing behavior at different nanofiller loadings. AFM analysis was also performed in the same manner as mentioned for the unfilled EEP film to investigate the depth of the cut recovered after healing (Fig. 5). At 2 wt% MXene concentration, the extent of healing was close to that of unfilled EEP. However, with further increases in filler loading (*i.e.* 5 and

10 wt%), a decrease in recovery was observed signifying the arrested motion of the S-IPN network. These results were consistent with the tensile properties (Fig. 4a and b), which demonstrated a considerable reduction in elongation at break at 5 and 10 wt% MXene loading signifying increasing stiffness.

The plausible mechanism behind the strong polymer–nanofiller interaction might be the formation of boronic ester linkages between the S-IPN and the surface hydroxyl group of MXene. In a previous study, we revealed the covalent bond formation between MXene and polyvinyl alcohol through boric acid.[49] A similar reaction might have occurred in this case between MXene and the free boronic acid end of some of the BDB molecules that were already attached to the S-IPN network (Fig. 1). To investigate the feasibility of boronic ester linkage formation, we treated the MXene with bis-boronic acid (f-MXene) only. In the FTIR spectra (Fig. 6a) of f-MXene, the transmittance peaks appeared at 1384 cm^{-1} (B–O stretching vibration), 1015 cm^{-1} (B–OH deformation vibration), 950 cm^{-1} (mild peak for –CH out of plane deformation), and 714 cm^{-1}
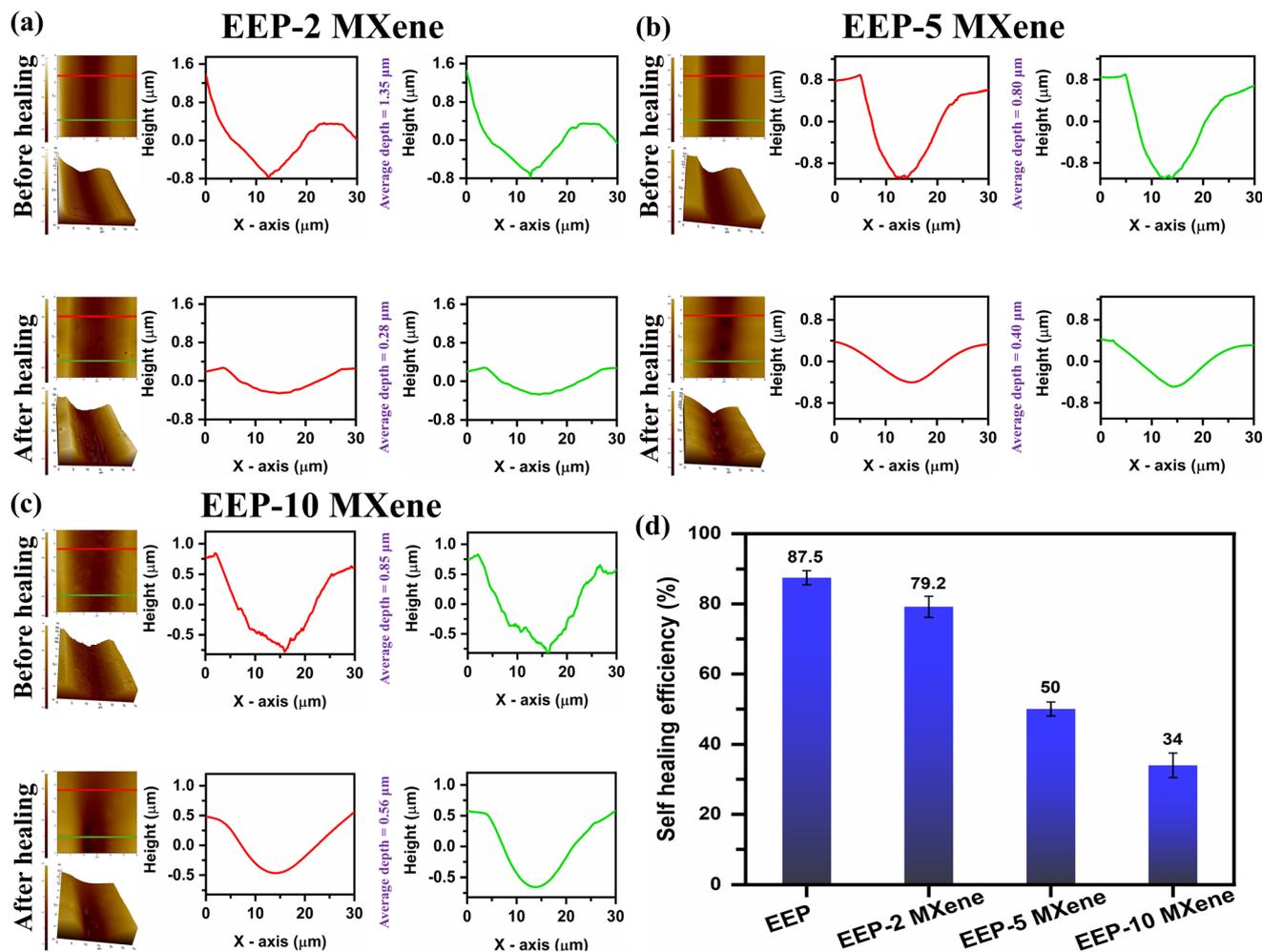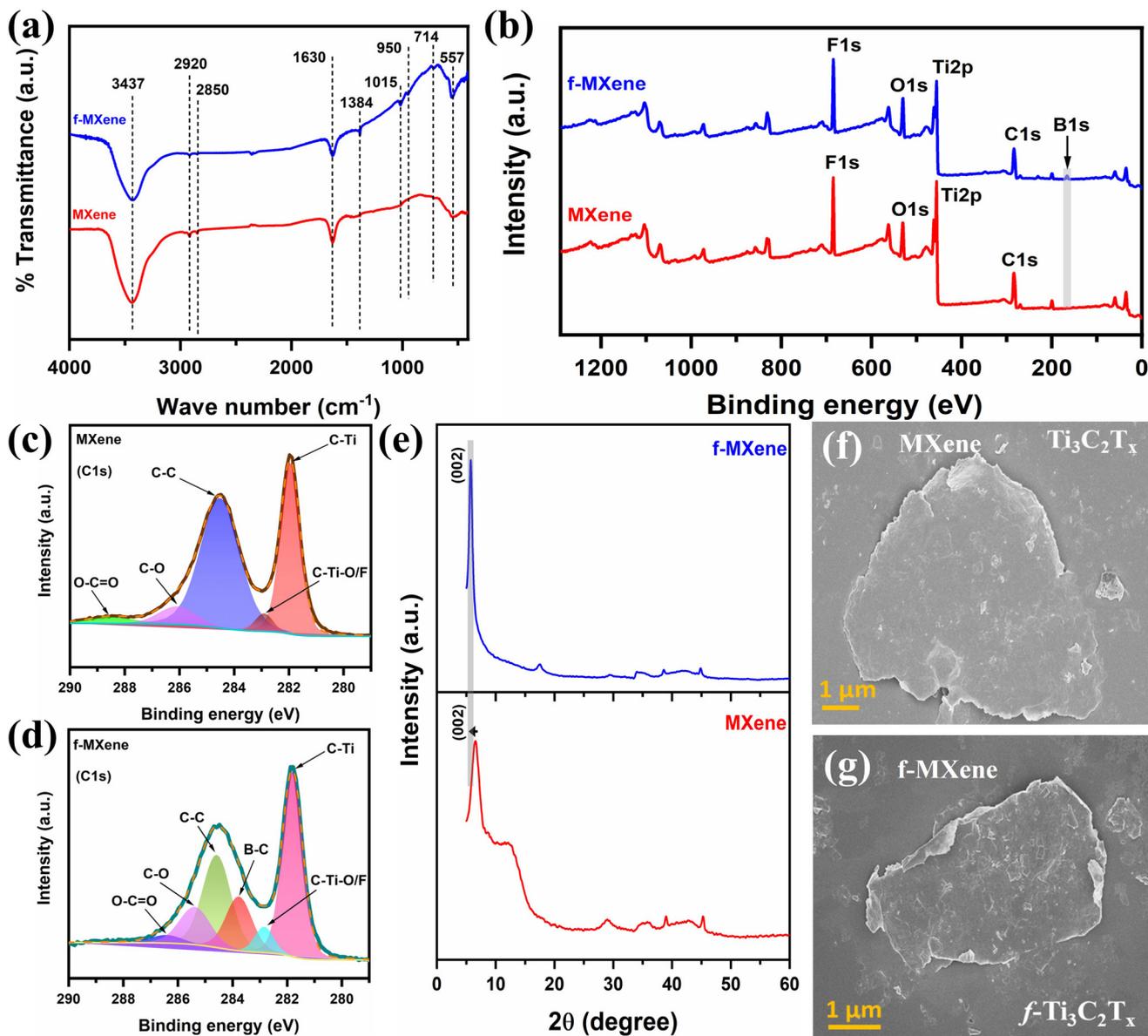

Fig. 5 AFM height images of the nanocomposite films before and after the healing test showing the depth of the damaged area: (a) EEP-2 MXene; (b) EEP-5 MXene; (c) EEP-10 MXene. (d) Comparison of the self-healing efficiency of the nanocomposites obtained from the depth of the damage recovered.

Fig. 6 (a) FTIR spectra of MXene and f-MXene; (b) XPS survey scan of MXene and f-MXene; (c) and (d) high-resolution C 1s spectra of MXene and f-MXene, respectively; (e) WAXD analysis of MXene and f-MXene; (f) and (g) FESEM scan images of MXene and f-MXene, respectively.

(out of plane benzene ring deformation) indicating the surface functionalization of MXene with the boronic acid group,[52,53] which were absent in the case of pristine MXene. Again, the XPS survey scan of f-MXene shown in Fig. 6b showed a peak at 199.2 eV corresponding to B 1s for f-MXene and the atomic wt% of B was found to be 1.08% (Table S1†).[54] While comparing the deconvoluted high-resolution C 1s spectra (Fig. 6c and d), f-MXene revealed an additional peak at 283.7 eV, which was attributed to the existence of the B–C bond in f-MXene.[55–57] Besides, the intensity of the peak ascribed to the C–C bond decreased after functionalization as compared to that of pristine MXene, which was attributed to the consumption of the C–OH group from the boronic ester moiety. Consequently, the C–O peak intensity showed an increase for f-MXene. A

reduction in the C–C peak intensity of MXene due to the interaction of the –OH group has also been reported in previous studies.[58] WAXD analysis indicated a shift of the peak representing the (002) plane towards a lower angle for f-MXene,[59] with respect to the untreated one (Fig. 6e). This signified an increase in the d-spacing from ~1.35 nm to ~1.54 nm due to the attachment of bis-boronic acid on the MXene inducing the layer separation. Edge folding of f-MXene was observed in the FESEM image when compared with the untreated MXene flake (Fig. 6f and g) also indicating that bis-boronic acid functionalization preferentially occurred at the edges of the MXene flake.[60] At the higher MXene loading, the extent of such linkage formation was expected to be higher, thus reducing the degree of healing in the nanocomposite films. To under-

stand the size distribution of the flakes, a low-magnification image of MXene is shown in Fig. S2.†

3.3 Properties of the nanocomposite coating

The representative images of the spray-coated nylon 6 substrates (thickness ~3.85 mm) are illustrated in Fig. S3.† It can be seen that there is a uniform distribution of the coating layer on the substrate surface. These coated samples were used for measuring the H_2GTR according to eqn (1), for all the S-IPN vitrimer nanocomposites at ambient temperature. The measured values are shown in Table 1, with the ancillary curves of H_2GTR $vs.$ time being shown in Fig. 7a and b. To calculate the permeability coefficient (P_1) using eqn (2), the thickness of the coating was measured by cross-sectional FESEM analysis, as shown in Fig. 7d and e. The H_2GTR value (or $J/\Delta P$) of the pristine nylon 6 substrate was 19.058 cm^3 m^{-2} d^{-1} atm^{-1}, which reduced to 0.84 cm^3 m^{-2} d^{-1} atm^{-1}, showing a 95.5% reduction after coating the nylon 6 with EEP. The reason behind this was stated to be the contribution of the dense interpenetrating network between epoxy chains and EVOH. The EVOH chain itself shows excellent gas-barrier properties.[13,61] On top of that, the formation of S-IPN while combining epoxy and EVOH reduced the free volume, showing an increase in T_g. The suppression of free volume hindered the diffusion of H_2 molecules, thus enhancing the barrier properties.[17] With the addition of 2 wt% MXene to the EEP composite, the H_2GTR decreased to a value of 0.59 cm^3 m^{-2} d^{-1} atm^{-1} with a permeability coefficient (P_1) of 0.062 cm^3 mm m^{-2} d^{-1} atm^{-1}. These values were further decreased with the addition of 5 and 10 wt% MXene to EEP exhibiting 0.17 and 0.03 cm^3 m^{-2} d^{-1} atm^{-1} H_2GTR with a permeability coefficient (P_1) values of 0.014 and 0.002 cm^3 mm m^{-2} d^{-1} atm^{-1}, respectively. A drastic ~99% reduction in the H_2GTR with 10 wt% MXene loading was observed, which is significant compared to the past results reported in the literature (Table S2†). The surface hydroxyl group of MXene could favor the polymer–filler interaction, leading to improved dispersion that introduces a long tortuous path for gas diffusion.

It was noticeable that the in $situ$ functionalization of MXene due to the presence of boronic acid while curing induced a strong polymer–filler network that acted as a nano-brick-layered architecture.[62] Thus, a long tortuous path was introduced for gas diffusion and H_2 permeability was further reduced for the nanocomposites. The tortuosity factor of the dispersed MXene was investigated using the following expression in eqn (3):[63]

$$R_p = \frac{P_c}{P_m} = \frac{1-\Phi}{\tau} \tag{3}$$

Here, R_p is the relative permeability, which indicates the ratio of the permeability coefficient of the nanocomposite coating (P_c) to the unfilled EEP coating (P_m). Φ represents the volume fraction of MXene, and τ is the tortuosity factor. According to the Bharadwaj model, τ can be expressed by the orientation parameter (f) as per the following equation:[63]

$$\tau = 1 + A\frac{\Phi}{3}(f+0.5) \tag{4}$$

Hence,

$$R_p = \frac{P_c}{P_m} = \frac{1-\Phi}{1+A\dfrac{\Phi}{3}(f+0.5)} \tag{5}$$

where A is the aspect ratio of the nanofiller, the value for which used was 500 as derived from the morphology analysis. The density of the MXene was taken as 3.7 g cm^{-3}.[64] The values of f were taken as 0 and 1 for random and parallel (aligned to the surface) orientation, respectively, in eqn (4) and (5). Fig. 7c compares the theoretical (R_p) considering parallel and random orientation values with the experimentally determined (R_p) at ambient temperature. Although the experimentally determined (R_p) at 2 wt% loading appeared to be near that for random orientation ($i.e.$ f = 0), it decreased with MXene concentration (5 and 10 wt%) showing experimental values closer to those for the parallel orientation. With the addition of MXene, the crystallinity of EVOH was impaired, which might not have been compensated for completely at 2 wt% MXene loading resulting in a permeability coefficient close to that of random orientation. However, it can be assumed that with a further increase in MXene concentration, parallel orientation was achieved with a strong polymer–filler

Table 1 Summary of the H_2GTR and permeability coefficient (P_1) values for the uncoated and coated nylon 6 substrates at ambient temperature

Sample designation	$l_1{}^a$ (mm)	$l_2{}^b$ (mm)	$(J/\Delta P)^c$ (H_2GTR)	P_2/L_2 ($P_2 = 19.058 \times 3.854$)	$P_1 = \dfrac{l_1}{\left[\dfrac{1}{\left(\dfrac{J}{\Delta P}\right)} - \left(\dfrac{l_2}{P_2}\right)\right]}{}^d$
Nylon 6		3.854	19.058	—	—
EEP	0.095	3.830	0.840	19.177	0.083
EEP-2 MXene	0.102	3.840	0.590	19.127	0.062
EEP-5 MXene	0.081	3.853	0.170	19.063	0.014
EEP-10 MXene	0.080	3.856	0.030	19.048	0.002

[a] Coating layer thickness on nylon 6. [b] Nylon 6 substrate thickness. [c] H_2GTR (cm^3 m^{-2} d^{-1} atm^{-1}) of the test sample. [d] Hydrogen gas permeability coefficient (cm^3 mm m^{-2} d^{-1} atm^{-1}) of the coating layer.
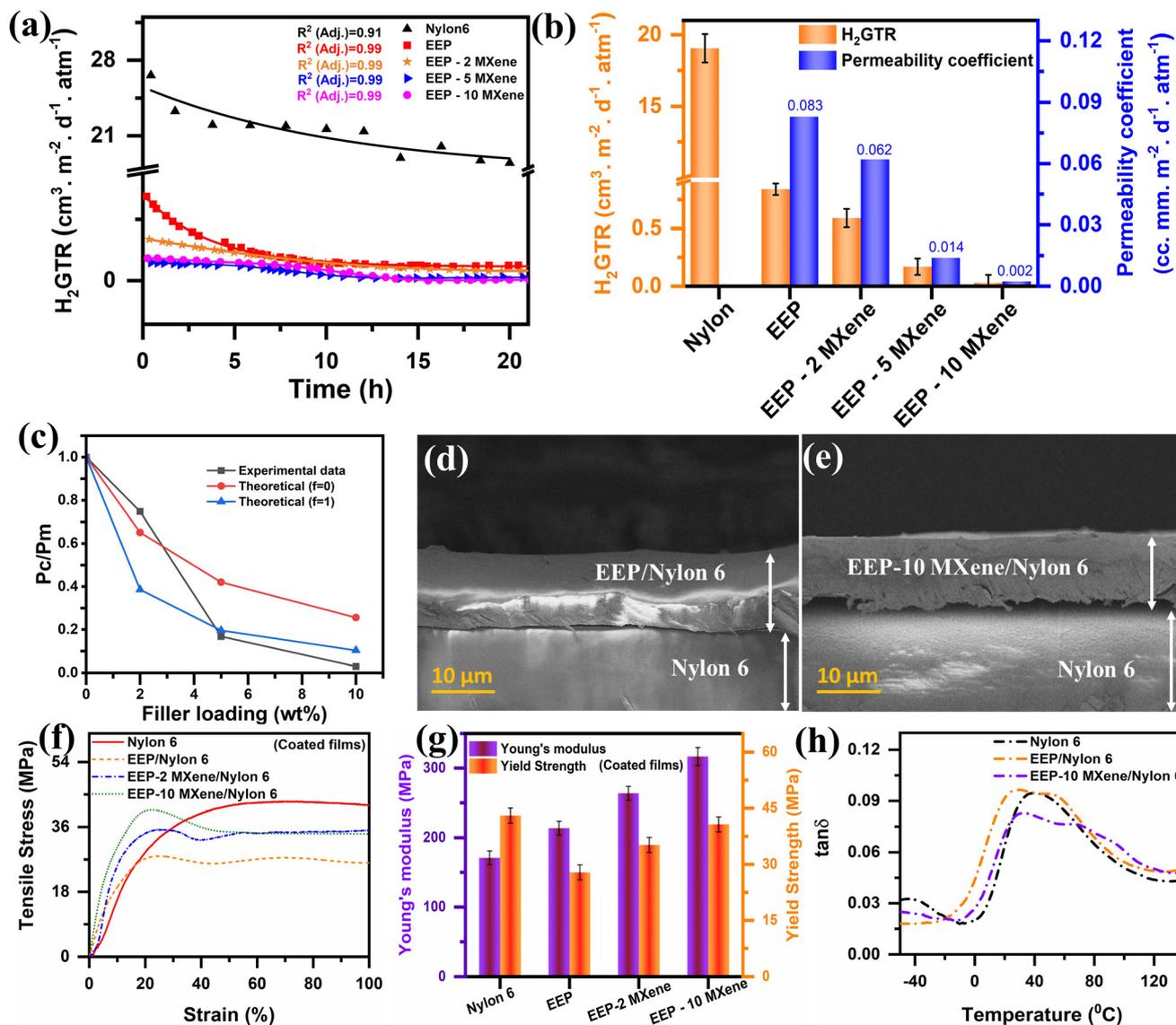
Fig. 7 (a) H_2GTR curves of uncoated and coated nylon 6 substrates at 25 °C; (b) summary of H_2GTR and permeability co-efficient values of the barrier coatings; (c) comparison between the experimental data and the Bharadwaj model for relative permeability at 25 °C; (d) and (e) cross-sectional FESEM images of representative coated nylon 6 substrates (EEP coating and EEP-10 MXene coating, respectively); (f) tensile stress–strain curves and (g) summary of mechanical properties of the coated films; (h) tan δ curves of the uncoated and coated nylon 6 films obtained from DMA.

network that fully compensated for the reduction in EVOH crystallinity. In addition to this, the Kubas-type interaction,[42] which entrapped the H_2 within the MXene layers, was also responsible for suppressing the H_2 permeability of the nanocomposites. Furthermore, we measured the H_2 permeability at 50 °C for the unfilled EEP-coated nylon 6 to understand the effect of temperature (Fig. S4†). An increase in permeability (H_2GTR, 2.14 cm³ m⁻² d⁻¹ atm⁻¹) was observed once the value stabilized between 17 and 20 h at 50 °C. However, the difference was not significant as the crosslinked network of the coating retained the structural integrity preventing H_2 diffusion.

We further measured the tensile modulus and T_g of the coated thin films to correlate with the barrier properties

(Fig. 7f–h). The coating (thickness less than 0.1 mm) applied to the 0.3 mm thick nylon 6 film increased the tensile modulus as compared to the uncoated nylon 6 film. With the filler loading, a gradual increase in the Young's modulus was observed as shown in Fig. 7f and g. The tan δ of the coated films showed two humps illustrating separate T_g values for the nylon 6 substrate and the coating layer (Fig. 7h). Comparing the T_g of the solvent-cast nanocomposites, it can be assumed that the tan δ peak at higher temperature represented the T_g of the coating while the lower temperature peak corresponded to the T_g of the nylon 6. A decrease in the T_g of the nylon 6 substrate in the case of the coated films might have resulted from thermo-oxidative degradation at the time of curing at elevated temperature.[65] However, the T_g of the coating was enhanced

along with the tensile modulus in the case of nanocomposite and thus indicated a stiffer coated film, which considerably suppressed H_2 diffusion. Furthermore, the peel-off test was also conducted to check the adhesion of the coating as this stands to be an essential parameter for confirming strong bonding between the coated layer and liner material in long-term applications. The peel-off test for the coated substrates of EEP and EEP-10 MXene was conducted using Scotch tape at room temperature (Fig. S5†). As per the ASTM standard D3359-17, the Scotch tape was peeled from the cut surface to check for any debonded surfaces from the coated layer of the substrate. No material from the coating layer came off depicting the adhesion of 5B classification as per the abovementioned ASTM standard. The water contact angle was measured to investigate the moisture sensitivity (Fig. S6†). Uncoated nylon 6 showed a lower contact angle (~70°) as it is sensitive to moisture. Compared to nylon 6, the EEP coating increased hydrophobicity (contact angle ~100°), although this is slightly impaired by the presence of MXene (contact angle ~90°), as expected. However, the developed coating is intended to be applied to the inner walls of pressure vessels and thus exposed to dry hydrogen only during application.

4 Conclusion

In this work, we have reported an epoxy vitrimer-based polymer nanocomposite coating as a barrier layer for the nylon 6 liner typically used in H_2 storage vessels. The barrier coating is comprised of an EVOH/epoxy reversibly crosslinked S-IPN, where the uncured epoxy monomer was treated with amine diol and boronic ester, enabling a dioxaborolane metathesis reaction to adopt a dynamic crosslinking network. The reversible S-IPN not only showed 87% self-healing efficiency, measured from the depth of recovery, but the tensile modulus also increased by ~81% as compared to that of pristine EVOH, which is conventionally used in barrier applications. The increase in modulus indicates restricted chain mobility, leading to the suppression of the free volume available for H_2 permeation as corroborated by an increase in T_g. Thus, the permeability was reduced by 95% in comparison with the uncoated nylon 6 substrate. The incorporation of MXene induced a strong polymer–filler network further restricting chain mobility and leading to higher modulus and T_g; however, healing efficiency was impaired as it depends on the molecular mobility. Up to 2 wt% MXene concentration, the self-healing efficiency did not significantly alter, while further increases in the MXene loading reduced the extent of healing. In contrast, gas permeability was continuously suppressed with increased MXene concentration. At 10 wt% MXene, a drastic 99% depletion in H_2GTR was noted with a healing efficiency of 30%, whereas 2 wt% MXene loading showed a 97% reduction in permeability along with considerable ~80% healing efficiency. While 10 wt% MXene made the coating almost impermeable to H_2, it also impaired the elongation at break or the toughness. Hence, the recommended loading of

the MXene would be less than 10 wt%. However, a hybrid filler approach could potentially improve both the toughness and barrier properties, which requires further investigation.

Author contributions

Anandarup Bhattacharyya: data curation, formal analysis, investigation, roles/writing – original draft. Subhabrata Saha: conceptualization, investigation, methodology, roles/writing – original draft, writing – review & editing. Sambedan Jena: investigation, methodology. Hoang Tuan Nguyen: methodology, investigation. Duy Thanh Tran: writing – review & editing, supervision, project administration. Nam Hoon Kim: supervision, project administration, roles/writing – original draft, writing – review & editing. Joong Hee Lee: writing – review & editing, supervision, project administration.

Data availability

The data that support the findings of this study are available from the corresponding author upon reasonable request.

Conflicts of interest

There are no conflicts to declare.

Acknowledgements

References

1 M. S. Dresselhaus and I. L. Thomas, *Nature*, 2001, **414**, 332–337.
2 P. Cotterill, *Prog. Mater. Sci.*, 1961, **9**, 205–301.
3 S. Villalonga, B. Gentilleau and D. Halm, *Int. J. Hydrogen Energy*, 2015, **40**, 13146–13147.
4 T. A. Yersak, D. R. Baker, Y. Yanagisawa, S. Slavik, R. Immel, A. Mack-Gardner, M. Herrmann and M. Cai, *Int. J. Hydrogen Energy*, 2017, **42**, 28910–28917.
5 R. K. Ahluwalia, T. Q. Hua and J. K. Peng, *Int. J. Hydrogen Energy*, 2012, **37**, 2891–2910.
6 Y. Sun, H. Lv, W. Zhou and C. M. Zhang, *Int. J. Hydrogen Energy*, 2020, **45**, 24980–24990.
7 G. Choudalakis and A. D. Gotsis, *Eur. Polym. J.*, 2009, **45**, 967–984.

8 S. Sinha Ray and M. Okamoto, *Prog. Polym. Sci.*, 2003, **28**, 1539–1641.

9 O. B. Seo, S. Saha, N. H. Kim and J. H. Lee, *J. Membr. Sci.*, 2021, **640**, 119839.

10 W. B. Park, P. Bandyopadhyay, T. T. Nguyen, T. Kuila, N. H. Kim and J. H. Lee, *Composites, Part B*, 2016, **106**, 316–323.

11 M. Safandowska, C. Makarewicz, A. Rozanski and R. Idczak, *Macromolecules*, 2022, **55**, 10077–10089.

12 J. M. Lagarón, E. Giménez, R. Gavara and J. J. Saura, *Polymer*, 2001, **42**, 9531–9540.

13 H. Wang, H. Zhang, B. Niu, S. Jiang, J. Cheng and S. Jiang, *RSC Adv.*, 2016, **6**, 29294–29302.

14 C. Habel, E. S. Tsurko, R. L. Timmins, J. Hutschreuther, R. Kunz, D. D. Schuchardt, S. Rosenfeldt, V. Altstädt and J. Breu, *ACS Nano*, 2020, **14**, 7018–7024.

15 X. Li, P. Bandyopadhyay, M. Guo, N. H. Kim and J. H. Lee, *Carbon*, 2018, **133**, 150–161.

16 M. W. Fitch, W. J. Koros, R. L. Nolen and J. R. Carnes, *J. Appl. Polym. Sci.*, 1993, **47**, 1033–1046.

17 S. Saha, W. Son, N. H. Kim and J. H. Lee, *J. Mater. Chem. A*, 2022, **10**, 4376–4391.

18 W. Son, S. Saha, D. T. Tran, N. H. Kim and J. H. Lee, *Carbon*, 2024, **228**, 119427.

19 M. Nakahata, Y. Takashima, H. Yamaguchi and A. Harada, *Nat. Commun.*, 2011, **2**, 511.

20 C. J. Kloxin and C. N. Bowman, *Chem. Soc. Rev.*, 2013, **42**, 7161–7173.

21 M. K. McBride, B. T. Worrell, T. Brown, L. M. Cox, N. Sowan, C. Wang, M. Podgorski, A. M. Martinez and C. N. Bowman, *Annu. Rev. Chem. Biomol. Eng.*, 2019, **10**, 175–198.

22 M. Rottger, T. Domenech, R. van der Weegen, A. Breuillac, R. Nicolay and L. Leibler, *Science*, 2017, **356**, 62–65.

23 F. Lossada, D. Jiao, D. Hoenders and A. Walther, *ACS Nano*, 2021, **15**, 5043–5055.

24 Y. Y. Jo, A. S. Lee, K.-Y. Baek, H. Lee and S. S. Hwang, *Polymer*, 2017, **108**, 58–65.

25 T. Liu, C. Hao, S. Zhang, X. Yang, L. Wang, J. Han, Y. Li, J. Xin and J. Zhang, *Macromolecules*, 2018, **51**, 5577–5585.

26 J. Xu, G. Wang, Y. Wu, X. Ren and G. Gao, *ACS Appl. Mater. Interfaces*, 2019, **11**, 25613–25623.

27 S. Talebian, M. Mehrali, N. Taebnia, C. P. Pennisi, F. B. Kadumudi, J. Foroughi, M. Hasany, M. Nikkhah, M. Akbari, G. Orive and A. Dolatshahi-Pirouz, *Adv. Sci.*, 2019, **6**, 1801664.

28 W. Xu, X. Zhou, Y. Fang, J. Xue, Q. Liu, Z. Chen, X. Xiong and J. Cui, *Adv. Funct. Mater.*, 2024, **34**, 2403681.

29 Y. Yang, F.-S. Du and Z.-C. Li, *ACS Appl. Polym. Mater.*, 2020, **2**, 5630–5640.

30 S. Cho, S. Y. Hwang, D. X. Oh and J. Park, *J. Mater. Chem. A*, 2021, **9**, 14630–14655.

31 S. Wang, X. Xing, X. Zhang, X. Wang and X. Jing, *J. Mater. Chem. A*, 2018, **6**, 10868–10878.

32 J. J. Cash, T. Kubo, A. P. Bapat and B. S. Sumerlin, *Macromolecules*, 2015, **48**, 2098–2106.

33 Y. Suzuki, D. Kusuyama, T. Sugaya, S. Iwatsuki, M. Inamo, H. D. Takagi and K. Ishihara, *J. Org. Chem.*, 2020, **85**, 5255–5264.

34 Y. Ito, D. Aoki and H. Otsuka, *Polym. Chem.*, 2020, **11**, 5356–5364.

35 D. R. Paul and L. M. Robeson, *Polymer*, 2008, **49**, 3187–3204.

36 P. A. Song, Y. Yu, T. Zhang, S. Fu, Z. Fang and Q. Wu, *Ind. Eng. Chem. Res.*, 2012, **51**, 7255–7263.

37 Y. Zhang, J. Tian, J. Zhong and X. Shi, *ACS Nano*, 2018, **12**, 10189–10200.

38 S. Tang, Z. Wu, X. Li, F. Xie, D. Ye, E. Ruiz-Hitzky, L. Wei and X. Wang, *Carbohydr. Polym.*, 2023, **299**, 120204.

39 K. Shi, X. Meng, S. Xiao, G. Chen, H. Wu, C. Zhou, S. Jiang and P. K. Chu, *Nanomaterials*, 2021, **11**, 2737.

40 L. Ding, Y. Wei, L. Li, T. Zhang, H. Wang, J. Xue, L. X. Ding, S. Wang, J. Caro and Y. Gogotsi, *Nat. Commun.*, 2018, **9**, 155.

41 C. V. Skipper, A. Hamaed, D. M. Antonelli and N. Kaltsoyannis, *Dalton Trans.*, 2012, **41**, 8515–8523.

42 B. Zheng, J. Li, L. Wang, H. Liu, J. Wang, L. Zhang and X. Chen, *Int. J. Hydrogen Energy*, 2024, **50**, 1555–1561.

43 J. M. S. Henis and M. K. Tripodi, *J. Membr. Sci.*, 1981, **8**, 233–246.

44 I. Pinnau, J. G. Wijmans, I. Blume, T. Kuroda and K. V. Peinemann, *J. Membr. Sci.*, 1988, **37**, 81–88.

45 L. Anderson, E. W. Sanders and M. G. Unthank, *Mater. Horiz.*, 2023, **10**, 889–898.

46 A. Kumar, Y. Lee, D. Kim, K. M. Rao, J. Kim, S. Park, A. Haider, D. H. Lee and S. S. Han, *Int. J. Biol. Macromol.*, 2017, **95**, 962–973.

47 W. Ge, S. Cao, F. Shen, Y. Wang, J. Ren and X. Wang, *Carbohydr. Polym.*, 2019, **224**, 115147.

48 Y. Shi, Y. Hong, J. Hong, A. Yu, M. W. Lee, J. Lee and M. Goh, *Composites, Part B*, 2022, **244**, 110181.

49 J. H. Woo, N. H. Kim, S. I. Kim, O.-K. Park and J. H. Lee, *Composites, Part B*, 2020, **199**, 108205.

50 S. Wan, X. Li, Y. Chen, N. Liu, Y. Du, S. Dou, L. Jiang and Q. Cheng, *Science*, 2021, **374**, 96–99.

51 S. Kang, H. Wang, M. Guo, L. Zhang, M. Chen, S. Jiang, X. Li and S. Jiang, *J. Agric. Food Ind.*, 2018, **66**, 13268–13276.

52 S. H. Brewer, A. M. Allen, S. E. Lappi, T. L. Chasse, K. A. Briggman, C. B. Gorman and S. Franzen, *Langmuir*, 2004, **20**, 5512–5520.

53 J. A. Faniran and H. F. Shurvell, *Can. J. Chem.*, 1968, **46**, 2089–2095.

54 R. K. Das and S. Mohapatra, *J. Mater. Chem. B*, 2017, **5**, 2190–2197.

55 M. F. Genisel, M. N. Uddin, Z. Say, M. Kulakci, R. Turan, O. Gulseren and E. Bengu, *J. Appl. Phys.*, 2011, **110**, 074906.

56 H. Ling, J. D. Wu, J. Sun, W. Shi, Z. F. Ying and F. M. Li, *Diamond Relat. Mater.*, 2002, **11**, 1623–1628.

57 M. O. Watanabe, T. Sasaki, S. Itoh and K. Mizushima, *Thin Solid Films*, 1996, **281–282**, 334–336.

58 Z. Zhao, S. Wang, F. Wan, Z. Tie and Z. Niu, *Adv. Funct. Mater.*, 2021, **31**, 2101302.

59 S. T. E., D. T. Tran, S. Jena, Y. Bai, S. Prabhakaran, D. H. Kim, N. H. Kim and J. H. Lee, *Chem. Eng. J.*, 2024, **481**, 148266.

60 J. E. Heckler, G. R. Neher, F. Mehmood, D. B. Lioi, R. Pachter, R. Vaia, W. J. Kennedy and D. Nepal, *Langmuir*, 2021, **37**, 5447–5456.

61 F. Yang, B. Li, Y. Li, Y. Duan, Y. Ding, Y. Xiong and S. Guo, *Chem. Eng. J.*, 2024, **481**, 148386.

62 P.-P. Xu, S. Yang, X.-R. Gao, S.-P. Chen, L. Xu, G.-J. Zhong, H.-D. Huang and Z.-M. Li, *Composites, Part B*, 2021, **222**, 109048.

63 R. K. Bharadwaj, *Macromolecules*, 2001, **34**, 9189–9192.

64 J. Yan, C. E. Ren, K. Maleski, C. B. Hatter, B. Anasori, P. Urbankowski, A. Sarycheva and Y. Gogotsi, *Adv. Funct. Mater.*, 2017, **27**, 1701264.

65 A. Bhattacharyya, N. Mishra, T. Dolui, J. Chanda, P. Ghosh and R. Mukhopadhyay, *J. Appl. Polym. Sci.*, 2022, **139**, e53148.